JOURNAL OF AIRCRAFT
Vol. 43, No. 6, November–December 2006

Aerodynamic Flow Control of an Airfoil with Small Trailing-Edge Strips

Deman Tang* and Earl H. Dowell†
Duke University, Durham, North Carolina 27708-0300

DOI: 10.2514/1.18969

The effects of small trailing-edge strips (Gurney flaps) on the steady and unsteady flow about a NACA0012 airfoil are computationally examined using a Navier–Stokes code, INS2D. Two Reynolds numbers, $Re = 107,000$ and 169,000, are used in the paper, the former corresponding to experiments previously reported in the literature and the latter corresponding to future proposed experiments. The computation of the unsteady flow includes an oscillating airfoil with several fixed Gurney flap sizes at higher angles of attack (beyond the stall angle of attack) and an oscillating Gurney flap with a fixed airfoil at higher angles of attack. For the former configuration, a correlation study between theory and a previous experiment has also been made. Reasonably good agreement with the experiment confirms the computational results that predict the effect of the Gurney flap is to enhance the maximum lift coefficient and stall angle of attack for both static and dynamic flows. The computations show that the effect of the Gurney flap is to move the separation position forward on the lower surface and back on the upper surface of the airfoil for near the trailing edge when the Gurney flap is oscillating. The oscillating Gurney flap increases the stall aerodynamic load.

Nomenclature

c	=	airfoil chord
C_d	=	drag coefficient
C_f	=	skin-friction coefficient
C_l	=	lift coefficient
C_m	=	pitching moment coefficient
C_p	=	pressure coefficient
$\hat{e}, \hat{f}$	=	convective terms in Navier–Stokes equation
$\hat{e}_v, \hat{f}_v$	=	viscous flux terms in Navier–Stokes equation
f_s	=	shedding frequency
h	=	Gurney flap height
J	=	Jacobian
p	=	pressure
$\hat{r}$	=	resistance
Re	=	Reynolds number
t, t^*	=	physical time, nondimensional time
ν	=	flow kinematic viscosity
α	=	angle of attack
β	=	artificial compressibility term
η	=	x-transformation coordinate
τ	=	pseudotime
ω, f	=	oscillating frequency, $\omega = 2\pi f$
ξ	=	y-transformation coordinate

Introduction

THE Gurney flap (GF) is a mechanically simple device consisting of a short strip located on the pressure side trailing edge of an airfoil, perpendicular to the chord. The first in-depth technical discussion of the flow around the Gurney flap was presented by Liebeck [1], although the Gurney flap was first used in the late 1960s by the American race car driver and team owner, Daniel Gurney. Liebeck showed that the Gurney flap increases the maximum lift coefficient and decreases the angle of attack of zero lift, whereas the lift curve slope remains relatively constant. Work in Refs. [2,3] studied the experimental aerodynamics of Gurney flaps on a single-element high-lift wing and on an airfoil. These experimental data indicate that there is a von Karman vortex sheet of alternately shed vortices present in the wake downstream of the Gurney flap, which increases both the suction and pressure on the suction and pressure sides of the airfoil. These two changes result in a larger pressure difference acting across the trailing edge and generate an increase in circulation. Reference [4] provides static experimental results for the lift enhancement of an airfoil using a Gurney flap and vortex generators. The addition of a Gurney flap increased the maximum lift coefficient from 1.49 to 1.96 and decreased the drag near the maximum lift condition for a NACA4412 airfoil. The application of vortex generators to the baseline airfoil yielded an increase in the maximum lift coefficient of 0.34.

Although the Gurney flap has been in use for some time, the published experimental and computational results do not fully describe the physics of the flow around the device nor do they provide a complete understanding of why the Gurney flap generates increases in lift both for static and dynamic stall.

The unsteady flow past an airfoil has been the subject of comprehensive reviews and surveys presented by McCroskey and others [5–8]. When the airfoil pitches through the static-stall angle of attack to higher angles of attack, the unsteady boundary layer separates and dynamic stall phenomena occur. In previous computations on oscillating airfoils, Aso and Hayashi [9] investigated the dynamic stall phenomena using two different numerical methods: a discrete vortex method and an incompressible Navier–Stokes solver. Both methods were capable of simulating the separated flows around an airfoil. Badcock et al. [10] computed the unsteady separated turbulent flow on an oscillating NACA0012 airfoil using a Navier–Stokes code. A pseudotime formulation of the Reynolds-averaged Navier–Stokes equation was used in their numerical method and yielded results that were in good agreement with the experiment.

These computational methods can also be used to study the management and control of the adverse effects of dynamic stall. Greenblatt and Wygnanski and others [11,12] have observed that both light and deep stall can be controlled using periodic excitation. They also observed that the periodic excitation was superior to steady blowing. All the previous experimental and computational studies have been with the airfoil oscillating in an oncoming steady flow. It is also of interest to study the fluid physics of an oscillating airfoil fitted with a fixed Gurney flap, as well as a fixed airfoil fitted with an oscillating Gurney flap beyond the static-stall angle of attack.

Received 28 October 2005; accepted for publication 10 February 2006.

*Research Associate Professor, Department of Mechanical Engineering and Materials Science.

†William Holland Hall Professor, Department of Mechanical Engineering and Materials Science. Member of the Center for Nonlinear and Complex Systems.

The present work focuses on the computational prediction for both the oscillating airfoil and the oscillating Gurney flap. An incompressible Navier–Stokes code, INS2D, developed at the NASA Ames Research Center, is employed. Reference [13] provides dynamic experimental results for an oscillating wing with small fixed trailing-edge strips (Gurney flaps). It is interesting to investigate the effect of Gurney flaps on the hysteresis observed in the aerodynamic-load loops of an oscillating airfoil. The present results may be helpful in better understanding the mechanism of lift enhancement and possible strategies for aerodynamic flow control.

Governing Equations

The governing equations for incompressible, constant density flow are written in conservative form with the density absorbed by the pressure term. The curvilinear coordinates are used in the form

$$\xi = \xi(x, y, t), \qquad \eta = \eta(x, y, t) \tag{1}$$

resulting in the following system of equations

Continuity equation

$$\frac{\partial}{\partial \xi}\left(\frac{U}{J}\right) + \frac{\partial}{\partial \eta}\left(\frac{V}{J}\right) = 0 \tag{2}$$

Momentum equation

$$\frac{\partial \hat{u}}{\partial t} = -\frac{\partial}{\partial \xi}(\hat{e} - \hat{e}_v) - \frac{\partial}{\partial \eta}(\hat{f} - \hat{f}_v) \equiv -\hat{r} \tag{3}$$

where $U = \xi_x u + \xi_y v$, $V = \eta_x u + \eta_y v$ and

$$\hat{u} = \frac{1}{J}\begin{bmatrix} u \\ v \end{bmatrix}$$

The time derivatives in the momentum equations are differenced using a second-order three-point implicit formula:

$$\frac{1.5\hat{u}^{n+1} - 2\hat{u}^n + 0.5\hat{u}^{n-1}}{\Delta t} = -\hat{r}^{n+1} \tag{4}$$

where the superscript n denotes the qualities at time $t = n\Delta t$ and $\hat{r}$ is the residual given in Eq. (3). To solve Eq. (4) for a divergence free velocity at the $n + 1$ time level, a pseudotime level τ is introduced and is denoted by a superscript m. The equations are iteratively solved such that $\hat{u}^{n+1,m+1}$ approaches the new velocity $\hat{u}^{n+1}$ as the divergence of $\hat{u}^{n+1}$ approaches zero. To drive the divergence of this velocity to zero, the following artificial compressibility relation is introduced:

$$\frac{\partial p}{\partial \tau} = -\beta \nabla \cdot \hat{u}^{n+1,m+1} \tag{5}$$

Applying an implicit Euler time differencing to Eq. (5) and rewriting Eq. (4) with the pseudotime superscripts gives

$$\frac{\hat{p}^{n+1,m+1} - \hat{p}^{n+1,m}}{\Delta \tau} = -\beta\left[\frac{\partial}{\partial \xi}\left(\frac{U}{J}\right) + \frac{\partial}{\partial \eta}\left(\frac{V}{J}\right)\right]^{n+1,m+1} \tag{6}$$

$$\frac{1.5\hat{u}^{n+1,m+1} - 1.5\hat{u}^{n+1,m}}{\Delta t} = -\hat{r}^{n+1,m+1} - \frac{1.5\hat{u}^{n+1,m} - 2\hat{u}^n + 0.5\hat{u}^{n-1}}{\Delta t} \tag{7}$$

where $\hat{p} = p/J$. Equations (6) and (7) can be iterated in both physical time and pseudotime to yield a converged solution. The pseudotime τ bears no relation to the physical time t. At each physical time step the equations are iterated in pseudotime. At convergence of the pseudotime iterations (called subiterations) the equations governing the unsteady flow are recovered. If we take Δt to be very large, such as $\Delta t = 10^{12}$, a converged solution for a steady-state flow can be obtained. For details about Eqs. (1–7), see Ref. [14].

Numerical Results

Steady-State Results for a Two-Dimensional Airfoil

Daniel Gurney first used Gurney flaps with the objective of creating more downforce on race cars, and other investigators subsequently used such flaps to improve the performance of commercial transport aircraft at transonic cruise conditions. For the present work, the Gurney flap is a short strip that is fitted perpendicularly to the pressure surface at the trailing edge of an airfoil. The typical Gurney flap height is 1–5% of the chord. In the present simulation, the airfoil has a NACA0012 cross section and is equipped with the 1.6, 2.5, and 3.2% chord height Gurney flap. Two Reynolds numbers of 107,000 and 169,000 are considered for light dynamic stall conditions. The incompressible Navier–Stokes code INS2D, developed at the NASA Ames Research Center, is employed. In the INS2D code the discretized equations are solved using a third-order upwind finite difference method and the solution is implicitly advanced using a Gauss–Seidel-type line relaxation.

The computational grids were generated using the GRIDGEN code. The grid points are clustered along the surface of the airfoil and the leading and trailing edges to better resolve the flow features in these regions. The C-O grid has dimensions of 438×100. The far-field boundaries are eight chord lengths from the airfoil.

The boundary conditions are specified as follows. The airfoil surface is a static, no-slip, wall boundary condition. The pressure is obtained by specifying a zero wall-normal pressure gradient. The far-field outer boundary is computed using a characteristic relation for

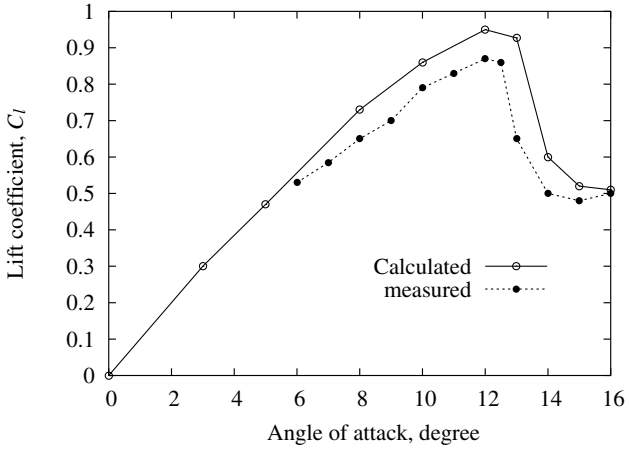

a) Lift coefficient

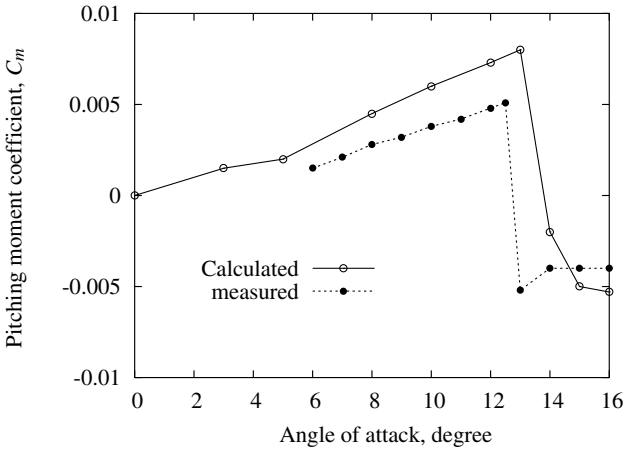

b) Pitching moment coefficient

Fig. 1 Comparison between calculation and experiment for the lift and pitching moment coefficients vs. angle of attack at $Re = 107,000$.

the pressure. At the downstream outflow boundary, a constant static pressure is used and the velocities are extrapolated from the interior. Along the wake-cut line of the C-grid, the pressure and velocities are obtained from an average of the surrounding values.

The Gurney flap is modeled by blanking out the grid points inside the flap. The surface of the flap is treated as a static, no-slip wall.

The lift and pitching moment coefficients for the baseline clean configuration are calculated. A comparison of the measured and calculated lift and pitching moment coefficients on the airfoil for angles of attack from 0 to 16 deg is shown in Figs. 1a and 1b, respectively. The measured data are provided by the authors of Ref. [13]. It can be seen that good correlation is observed between computation and experiment except near the maximum lift and pitching moment coefficients.

The lift and drag coefficients for different Gurney flap heights are presented in Figs. 2a and 2b for angles of attack from 0 to 16 deg and Gurney flap heights from 1.6 to 3.2% of the chord. For comparison, the results for the baseline clean configuration are also plotted in these figures. It can be seen that the addition of the Gurney flap produces a significant lift and pitching moment coefficient increment compared with the baseline configuration.

Typical pressure distribution along the upper and lower surfaces are shown in Figs. 3a and 3b, for a smaller incidence (less than the static-stall angle) $\alpha = 5$ deg and for a larger incidence (greater than the static-stall angle) $\alpha = 15$ deg, respectively. For the case without the Gurney flap, there is a little greater lift at 5 deg than at 15 deg. For the case with the Gurney flap, the pressure change is significant both for smaller and larger incidences, especially near the trailing region for the larger incidence. The effect of the Gurney flap is to increase the pressure on the surface of the airfoil compared with the clean airfoil case. Comparing to Figs. 3a and 3b for the addition of the Gurney flap, the results show a significant pressure increase in the leading edge suction peak for a small incidence $\alpha = 5$ deg (smaller than the static-stall angle of attack). This is because of an increased circulation at the trailing edge due to the Gurney flap. But for a larger incidence $\alpha = 15$ deg (larger than the static-stall angle of attack), the increase is not as significant due to the stall flow and reduced circulation.

The flow velocities, u and v in the x and y directions, around the airfoil surface and near the airfoil surface region are dependent on the incidence, the Reynolds number, the Gurney flap motion, and other factors. The flow separation point position on the airfoil surface and the separation bubble phenomenon are sensitive to computational model details. The Spalart–Allmaras turbulence model is used in the INS2D code. By definition, in those regions of the flow field where separation is said to occur, both the x-component u and the y-component v of the flow velocity are less than or equal to zero. The results are shown in Figs. 4 and 5.

In the case without the Gurney flap, when $\alpha = 5$ deg, no flow reversal is observed as shown in Fig. 4a. Trailing-edge flow reversal is first observed at $\alpha = 10$ deg. As α increases, the flow reversal regions are more elongated and exist at both the trailing and the leading edges. Typical results are shown in Fig. 4b for $\alpha = 12$ deg. Note the latter flow reversal region is larger than the former. When α increases from $\alpha = 12$ deg to $\alpha = 20$ deg as shown in Fig. 4c, the flow reversal region enlarges.

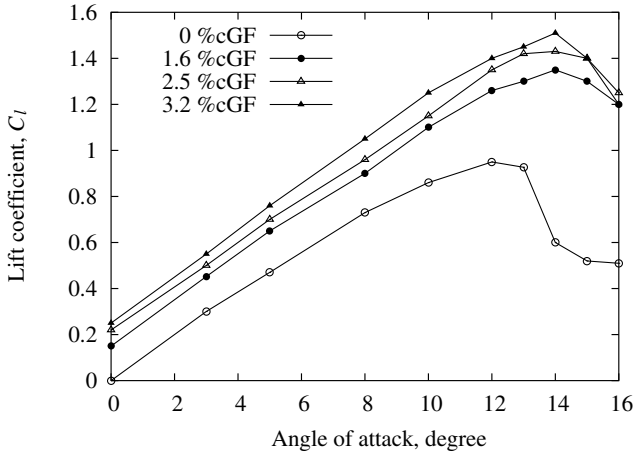

a) Lift coefficient

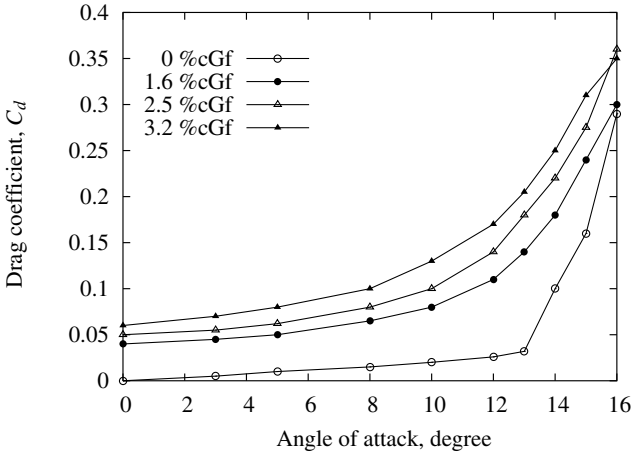

b) Drag coefficient

Fig. 2 Effect of Gurney flap heights on the static aerodynamics at $Re = 107,000$.

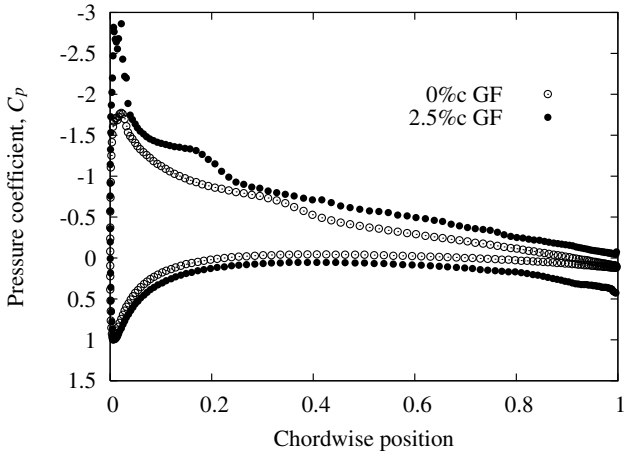

a) $\alpha = 5$ deg

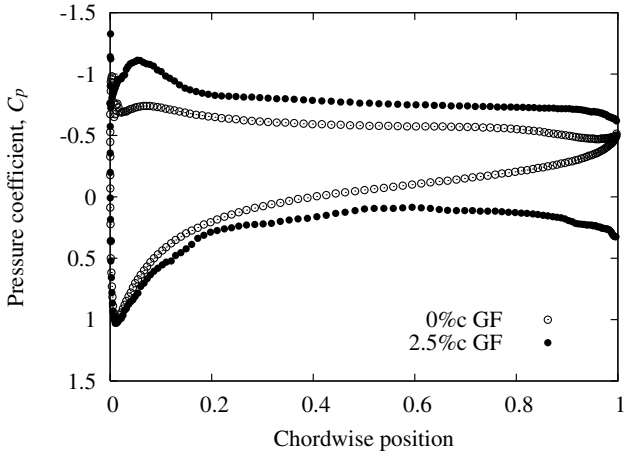

b) $\alpha = 15$ deg

Fig. 3 Pressure coefficient C_p vs. x/c at $\alpha = 5$ and 15 deg at $Re = 107,000$ for $0\%c$ Gurney flap and for $2.5\%c$ Gurney flap.

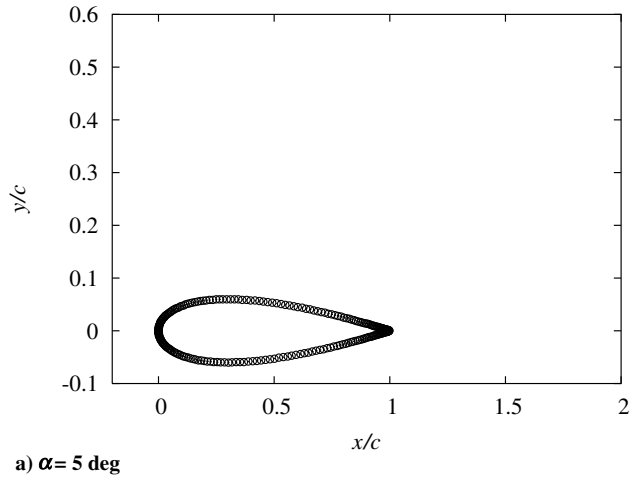

a) $\alpha = 5$ deg

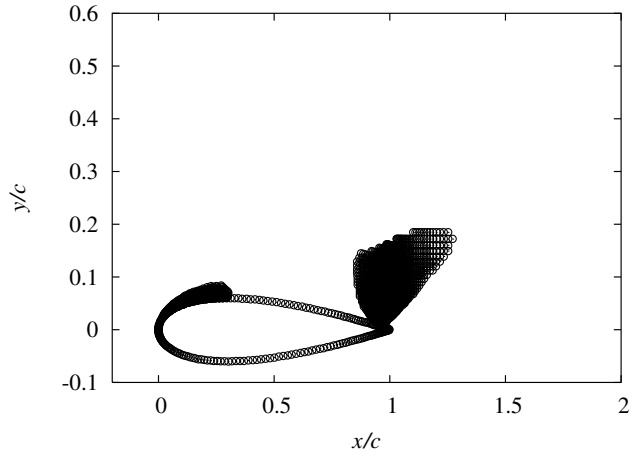

b) $\alpha = 12$ deg

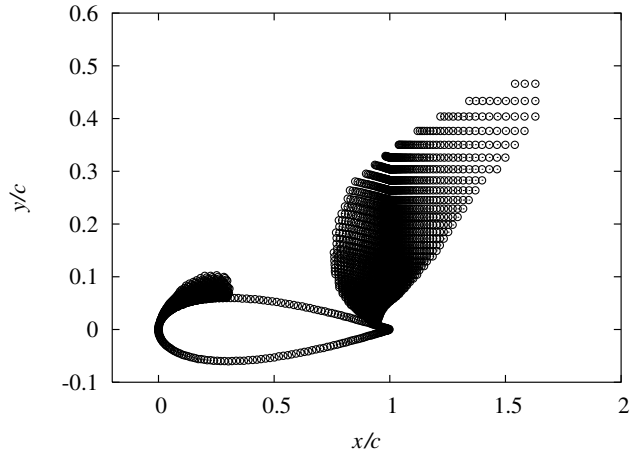

c) $\alpha = 20$ deg

Fig. 4 Flow reversal spread regions for $\alpha = 5$, 12, and 20 deg at $Re = 107,000$, for $0\%c$ Gurney flap. Note the y/c scale has been exaggerated for clarity.

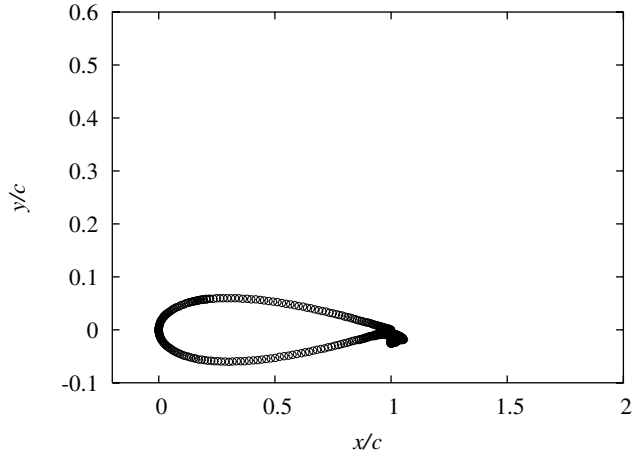

a) $\alpha = 5$ deg

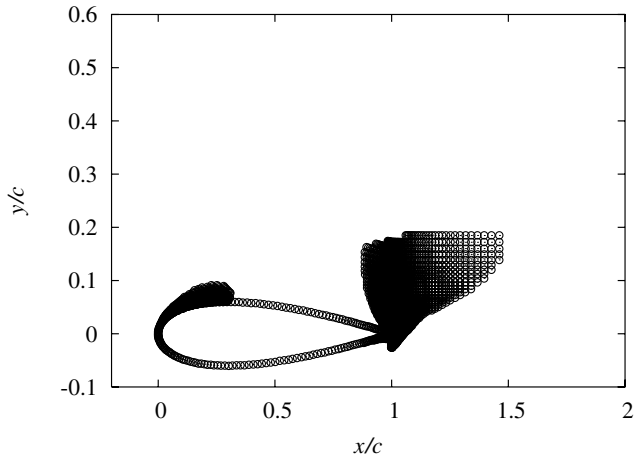

b) $\alpha = 12$ deg

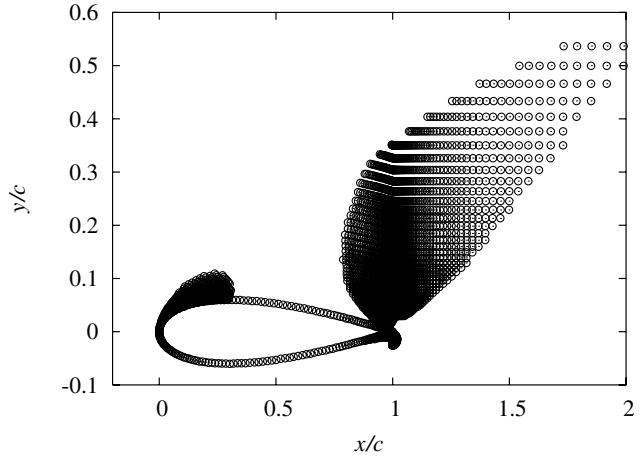

c) $\alpha = 20$ deg

Fig. 5 Flow reversal spread regions for $\alpha = 5$, 12, and 20 deg at $Re = 107,000$, for $2.5\%c$ Gurney flap. Note the y/c scale has been exaggerated for clarity.

In the case with the Gurney flap, when α is small, such as $\alpha = 5$ deg as shown in Fig. 5a, the flow reversal region occurs only near the Gurney flap, but it still influences the pressure distribution along the chord as shown in Fig. 3b. When α increases to $\alpha = 12$ deg as shown in Fig. 5b, both leading and trailing-edge flow reversal regions are observed. For larger α, the pressure change is mainly near the trailing region as shown in Fig. 3b. Results for $\alpha = 20$ deg are plotted in Fig. 5c. A very large flow reversal region is observed near the trailing edge. It significantly affects the pressure distribution on the airfoil surface and stall aerodynamic performance.

For the steady-state aerodynamics of a two-dimensional airfoil, there are four points to be noted:

1) When the angle of attack is zero, there is a nonzero lift and the lift coefficient increases as Gurney flap height increases. This is because there is an additional circulation due to a von Karman vortex street of alternately shed vortices created by the Gurney flap near the trailing edge. Figure 6 shows the contours of vorticity for $\alpha = 0$ deg and a Gurney flap height of 3.2% of the chord. As shown in this figure

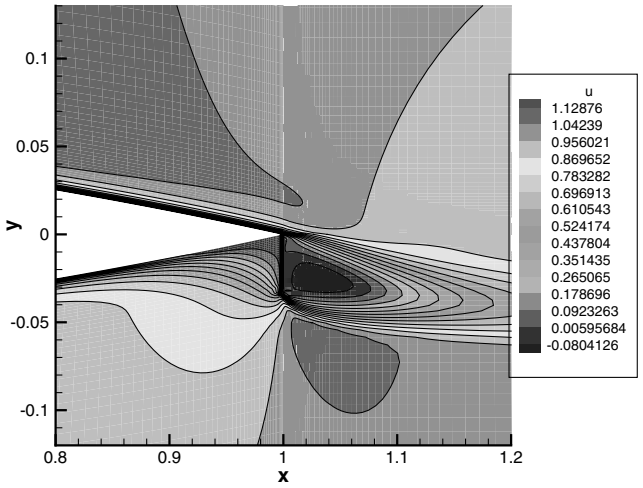

Fig. 6 The u contour for an airfoil with a Gurney flap height of 3.2%c at $Re = 107,000$ and $\alpha = 0$ deg.

there are two distinct counter-rotating vortices directly downstream of the Gurney flap where the streamlines bounding the vortex region meet. This pattern is consistent with that first hypothesized by Liebeck [1] and the measured data of Jeffrey et al. [2].

2) The static-stall angle increases due to the Gurney flap compared with the clean airfoil. These results are consistent with the experimetal data [3], which used an NLF(1)-0414F section shape and $Re = 1.1 \times 10^6$. For the present baseline airfoil, the static-stall angle is about 13 deg. With the Gurney flap, the static-stall angle is about 14 deg.

3) The addition of a Gurney flap increases the maximum lift coefficient from 0.95 up to 1.58 for 1.6%c GF, 1.7 for 2.5%c GF, and 1.75 for 3.2%c GF. As shown in Fig. 6, the additional increase in circulation in the trailing-edge region increases the total lift coefficient of the airfoil.

4) With the addition of a Gurney flap, there is a significant drag penalty as shown in Fig 2b. A larger Gurney flap height leads to a larger drag coefficient.

Unsteady-State Results for a Two-Dimensional Airfoil

Oscillating Airfoil with a Fixed Gurney Flap

The unsteady two-dimensional equations are solved in generalized coordinates for unsteady flow. The method of artificial compressibility is used to couple the continuity equation with the momentum equation. In this method a physical time derivative of pressure is added to the continuity equation. Note the difference between the physical time t and a pseudotime τ in the original equations. At each physical time step the original momentum equation is iterated in pseudotime. At convergence of the pseudotime iterations (subiterations) the equations governing the unsteady flow are recovered.

The artificial compressibility constant β was set to 10 and the pseudotime step $\Delta\tau$ was set to 10^{12}. Each subiteration in pseudotime was converged until the maximum divergence of velocity at any point was less than 10^{-4}. The maximum subiteration number was taken to be 1000.

The airfoil pitch oscillation about the 0.25 chord location is expressed as

$$\alpha(t) = 11\,\text{deg} + 5\,\text{deg}\ \sin 2\pi f t \tag{8}$$

A reduced frequency $k = \pi f c/U_\infty = 0.05$ with a Reynolds number $Re = 107,000$ are used in both the computation and previous experiment [13]. The model chord is $c = 0.15$ (m), the flow velocity is $U_\infty = 11.05$ m/s, and the oscillation frequency is $f = 1.173$ Hz.

The oscillating angle of attack can be expressed in a discrete numerical form as

$$\Delta\alpha(t) = 5\,\text{deg}\ \sin i2\pi f \Delta t, \qquad i = 1, 2, \ldots N_t \tag{9}$$

For one period of the airfoil oscillation,

$$\Delta t = \frac{1}{f N_t} \tag{10}$$

where N_t is the total number of the time steps. Here $N_t = 79$ is chosen and the time step is $\Delta t = 0.0108$.

A sequence of 40 grids, each corresponding to the NACA0012 airfoil at certain angles of attack for pitch-up from -5 deg to $+5$ deg, were generated. Another 39 grids for pitch-down from 4.96 deg to -5 deg can be determined from the former 40 grids. Because of the equal time steps, the increment of the angle of attack is nonuniform for the grid sequence. The INS2D code read in a new grid at the beginning of each time step so that the pitch sinusoidal motion of the airfoil could be simulated. For executing the time-step iteration, a batch-run file is needed. In this file it is necessary to specify the relationship between the input and output files. For the first time step, the number of time steps $N_{t\max}$ should be larger than N_t in the first input file; that is, the steady dynamic response is achieved through both the real time and pseudotime subiteration process due to static flow initial conditions. After the first time-step, $N_{t\max} = 1$ in the other input file; that is, the steady dynamic response is achieved through the pseudotime subiteration process due to dynamic flow initial conditions.

Three Gurney flap heights, 0, 1.6, and 3.2%c are considered for both the theory and experiment. The first case is the baseline oscillating airfoil. The theoretical and experimental correlation for the dynamic-lift loops of an oscillating airfoil is shown in Fig. 7a for the baseline oscillating airfoil, Fig. 7b for 1.6%c GF, and Fig. 7c for 3.2%c GF. The experimental results are provided by the authors of Ref. [13]. The reader can find a description of the details of the experimental technique and measured data in this reference.

As shown in Fig. 7a for the baseline oscillating airfoil, a large hysteresis in the dynamic-lift loop is clearly seen in both the theoretical and experimental results. The results are very similar to those shown in Refs. [7,9]. A 41.4% increase in $C_{l,\max} = 1.24$ at a dynamic-stall angle and $\alpha_{ds} = 15.15$ deg is found, compared with $C_{l,\max} = 0.877$ and $\alpha_{ds} = 12.5$ deg for the static lift curve (Fig. 2) in the experiment. By comparison, a 14.7% increase in $C_{l,\max} = 1.09$ at a dynamic-stall angle and $\alpha_{ds} = 14.6$ deg is found, compared with $C_{l,\max} = 0.95$ and $\alpha_{ds} = 12.0$ deg for a static lift curve (Fig. 3) from the theory. The correlation between the theory and experiment is generally good except for the maximum dynamic lift.

As shown in Fig. 7b, with the addition of a Gurney flap with 1.6%c height there is an increase in the effective camber and a shift in the dynamic-lift curve upward. The maximum dynamic lift is $C_{l,\max} = 1.3956$ at a dynamic-stall angle and $\alpha_{ds} = 14.86$ deg in the experiment. By comparison, a 11.7% increase in $C_{l,\max} = 1.5$ at a dynamic-stall angle and $\alpha_{ds} = 13.02$ deg is found, compared with $C_{l,\max} = 1.35$ and $\alpha_{ds} = 14.0$ deg for a static lift curve (Fig. 2) from the theory. The correlation between the theory and experiment is reasonably good except in the region of higher angle of attack.

Figure 7c shows the dynamic-lift loop for a Gurney flap with 3.2%c height. The maximum dynamic lift is $C_{l,\max} = 1.56$ at a dynamic-stall angle and $\alpha_{ds} = 13.95$ deg in the experiment. By comparison, a 17.8% increase in $C_{l,\max} = 1.78$ at a dynamic-stall angle and $\alpha_{ds} = 14.05$ deg is found, compared with $C_{l,\max} = 1.51$ and $\alpha_{ds} = 14.0$ deg for a static lift curve (Fig. 2) from the theory. The correlation between the theory and experiment is reasonably good except for the regions of the highest and lowest angles of attack.

Both the theoretical and experimental results indicate there is a lift coefficient improvement throughout the entire oscillation cycle compared with a baseline airfoil with no Gurney flap and the maximum dynamic lift increases as the Gurney flap height increases.

The dynamic stall process is initiated by turbulent flow separation at the leading edge and flow reversal near the trailing edge, which causes the asymmetry between the flow separation and reattachment when the oscillation is pitch-up and pitch-down. The addition of the Gurney flap (adding an additional circulation at the trailing edge) delays boundary-layer separation and increases the maximum dynamic-lift coefficient.

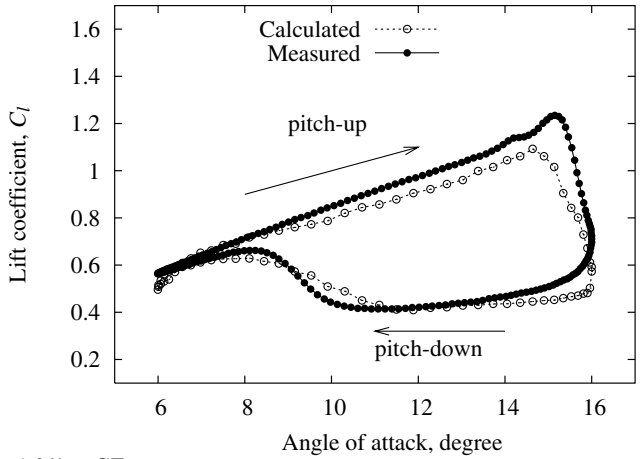

a) 0%c = GF

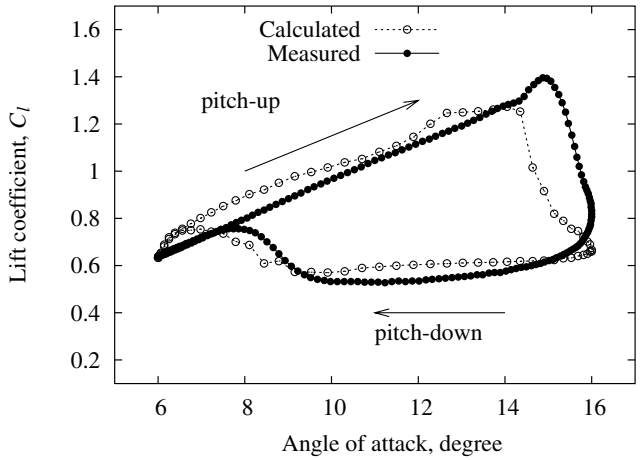

b) 1.0%c = GF

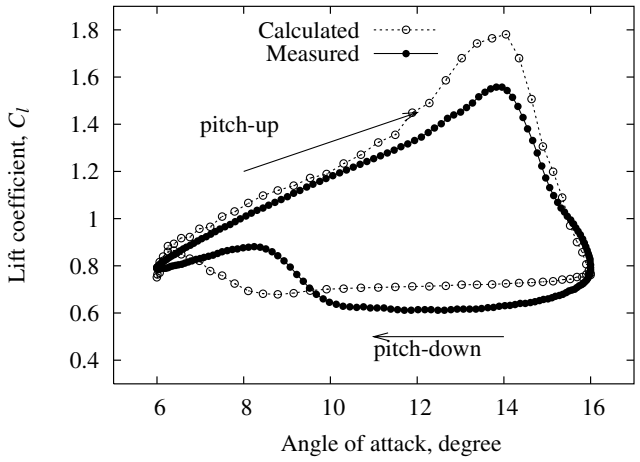

c) 3.2%c = GF

Fig. 7 Effect of Gurney flap heights on the dynamic-lift loops at $Re = 107,000$.

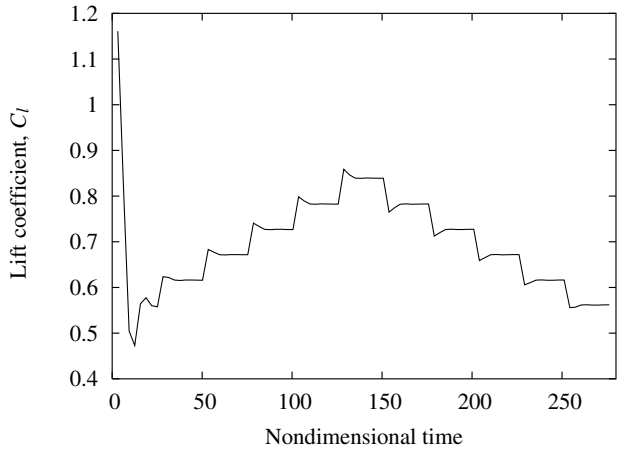

a) For $N_t = 10$

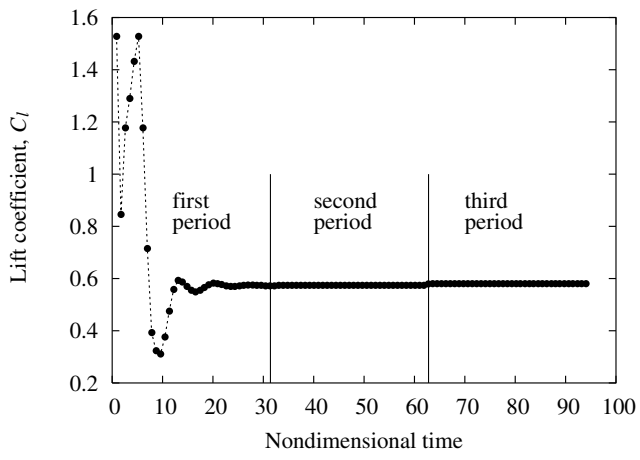

b) For $N_t = 40$

Fig. 8 Time histories of the lift coefficient response for $\alpha = 15$ deg at $Re = 169,000$.

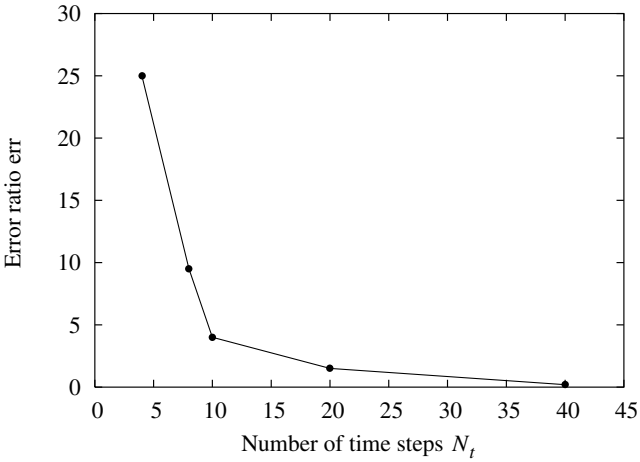

Fig. 9 Percent error err vs. the number of time steps N_t for hyperbolic excitation of the Gurney flap.

Oscillating Gurney Flap with a Fixed Airfoil

An oscillating Gurney flap is located at the trailing edge of the low airfoil surface. The Gurney flap airfoil oscillation is given by

$$h(t) = \frac{h_0}{2}\left[1 + \sin\left(\frac{3\pi}{2} + \omega t\right)\right] \tag{11}$$

where h_0 is the maximum oscillating amplitude of the Gurney flap.

The chord length of the airfoil is $c = 0.254$ (m). The maximum oscillating amplitude of the Gurney flap is $h_0 = 2.5\%c$ and the oscillating frequency is $\omega = 7.65$ rad/s. Two oscillating excitation functions are considered. One is a hyperbolic time function that is called case 1. Another is an approximate sinusoidal time function that is called case 2. This is an approximation because the airfoil grid distribution along the y axis is hyperbolic. The boundary conditions for the Gurney flap cannot form an exact sinusoidal function, but can form an approximate sinusoidal function. The chosen physical time step Δt is dependent on the oscillating frequency ω and the number

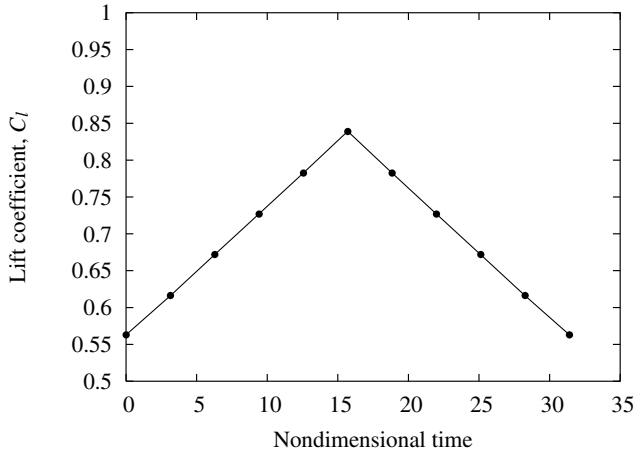

a) Lift coefficient

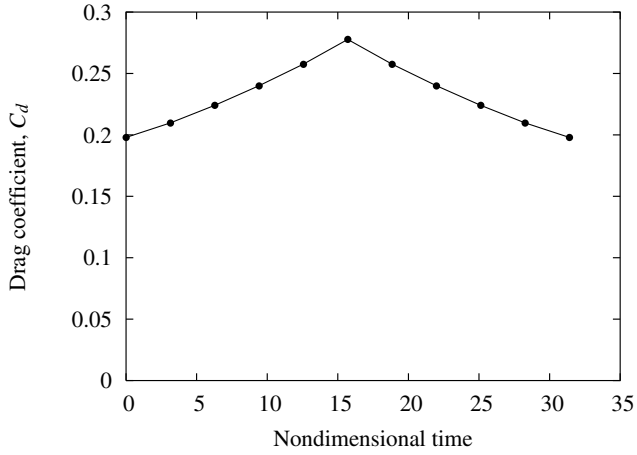

b) Drag coefficient

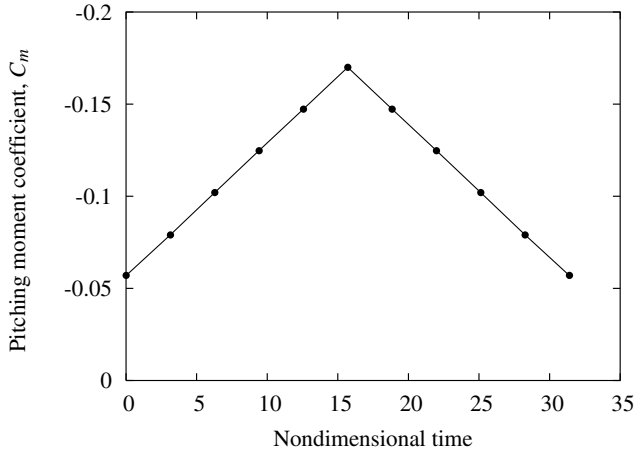

c) Pitching moment coefficient

Fig. 10 Force response amplitude for $\alpha = 15\,\text{deg}$ at $Re = 169,000$.

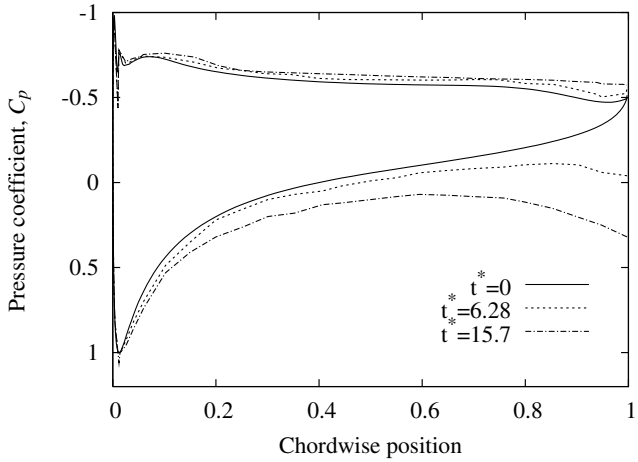

a) Pressure coefficient

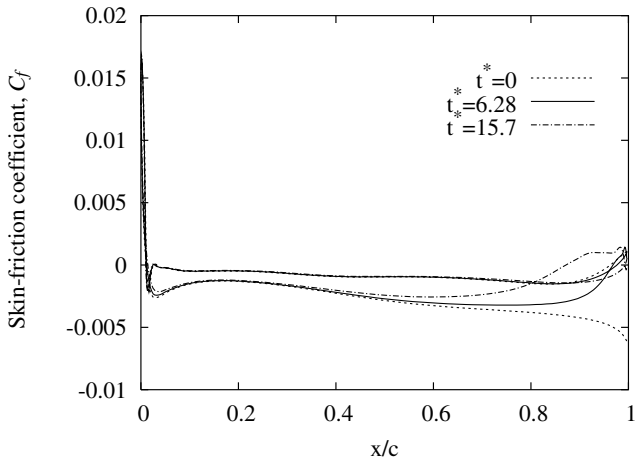

b) Skin friction coefficient

Fig. 11 Pressure and skin-friction responses for $\alpha = 15\,\text{deg}$ at $Re = 169,000$.

of time steps N_t used for one period of the oscillation as shown in Eq. (10).

A Reynolds number of $Re = 169,000$ (corresponding to planned future experiments) is considered for the present unsteady-state flow calculations. As described in the INS2D code, the nondimensional time t^* is normalized by $\frac{c^2}{\nu Re}$. For case 1, $N_t = 10$ and the nondimensional time step is $\Delta t^* = 3.14$, and for case 2, $N_t = 36$ and the nondimensional time step is $\Delta t^* = 0.8713$.

As discussed for the oscillating airfoil case, a sequence of grids is generated, each corresponding to a certain angle of attack before running the INS2D code. For the present case, the airfoil is fixed at a certain angle of attack while the Gurney flap oscillates. Here a new alternate computational method is proposed. A sequence of several boundary condition files (bcmain.dat), each corresponding to a specific Gurney flap amplitude at the angle of attack of 15 deg, was generated. The INS2D code read in a new boundary condition file at each time step and a new initial condition for the pseudotime iteration was created by the converged response of the previous physical time step. This iteration process is automatically executed by a batch-run file. However, when reading in a new boundary condition file at each physical time step, there is a physical time transient vibration process. This means that for each new boundary condition, the physical time response is different but these satisfy the convergent conditions of the pseudotime subiteration. Thus the forces or pressure response on the airfoil surface to the Gurney flap oscillating motion is complex. To evaluate the present method, the hyperbolic time function excitation (case 1) is used. This case is chosen because the excitation amplitude is exact for the present hyperbolic airfoil grid distribution.

The effect of the transient response process on the steady response amplitude is considered when different numbers of time steps are considered. Figure 8a shows the time history of lift coefficient C_l vs. the nondimensional physical time for $\alpha = 15\,\text{deg}$. Reading each boundary condition file that corresponds to each time step of the Gurney flap oscillation, ten ($N_t = 10$) physical time steps are used for each period of Gurney flap motion. During each time step, the Gurney flap amplitude is held constant and there is no change to the airfoil grid. For the first boundary condition file input, the transient lift response process in physical time is quite long, that is, the steady

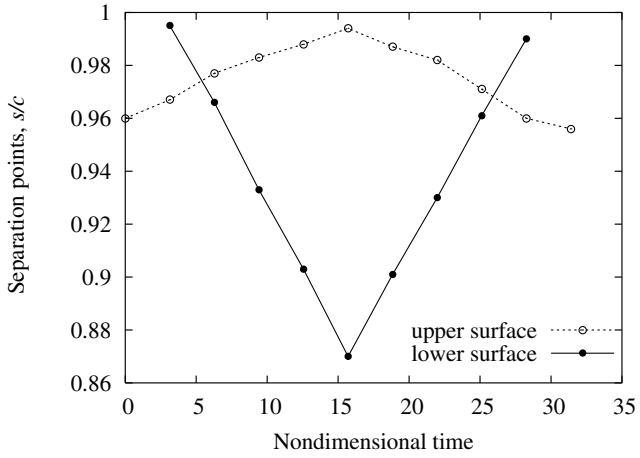

a) Near trailing edge

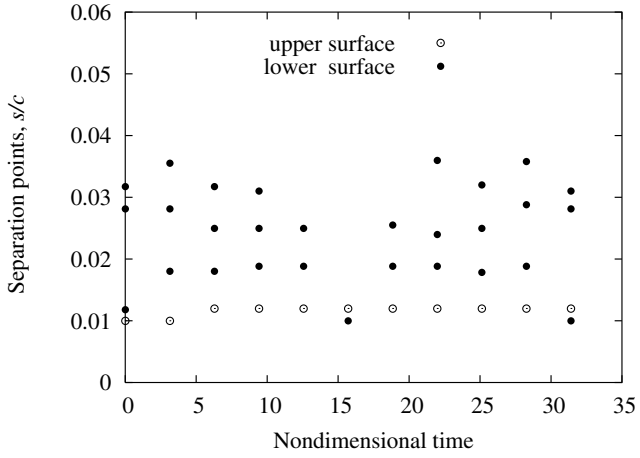

b) Near leading edge

Fig. 12 Unsteady boundary-layer separation for $\alpha = 15\,\mathrm{deg}$ at $Re = 169,000$.

response is reached after eight time steps; see Fig. 8a for the nondimensional time region from $t^* = 0$ to $t^* = 31.4$. This is because the initial conditions are from a state of quiescent flow, that is, no mean flow. After the second boundary condition file input, the transient process becomes short, but there is still a detectable artifact of the numerical method. This is because the time step Δt^* chosen is too large, that is, only 11 points per period of airfoil oscillation. After a first period of airfoil oscillation, we define an error percent ratio:

$$\mathrm{err} = \frac{A_1 - A_{\mathrm{steady}}}{A_{\mathrm{steady}}}\,\%$$

where A_1 is an amplitude corresponding to the first time step of each oscillation period, that is, $N_{t\max} = 1$ is the input file and A_{steady} is an amplitude corresponding to the steady amplitude of each oscillation period. For the preceding example, the averaged err is about 4.0%. When the number of time steps (N_t for one period of oscillation) increases to $N_t = 40$, the results are shown in Fig. 8b for the first three periods. It is seen that err is almost zero. A numerical test for a different N_t in the preceding example is made. The results of the error percent ratio vs. the number of time steps N_t are shown in Fig. 9. In all subsequent calculations, $N_t = 10$ was used.

The aerodynamic force responses to the Gurney flap oscillation are shown in Figs. 10a and 10b for the drag coefficient and Fig. 10c for the pitching moment coefficient.

The instantaneous surface pressure coefficients C_p are shown in Fig. 11a for the nondimensional times $t^* = 0$, 6.28, and 15.7 of the Gurney flap oscillating excitation. When the Gurney flap amplitude

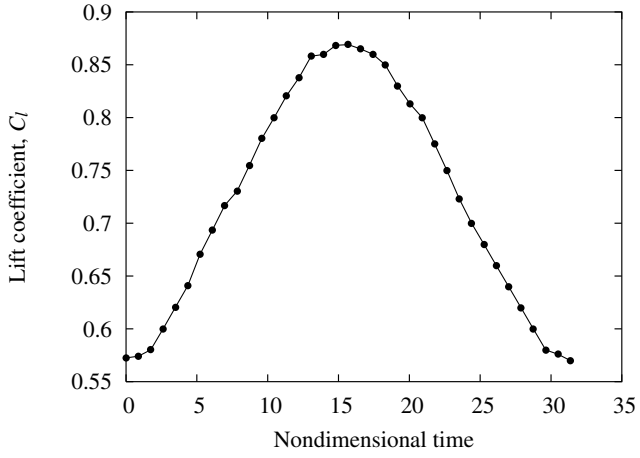

a) Lift coefficient

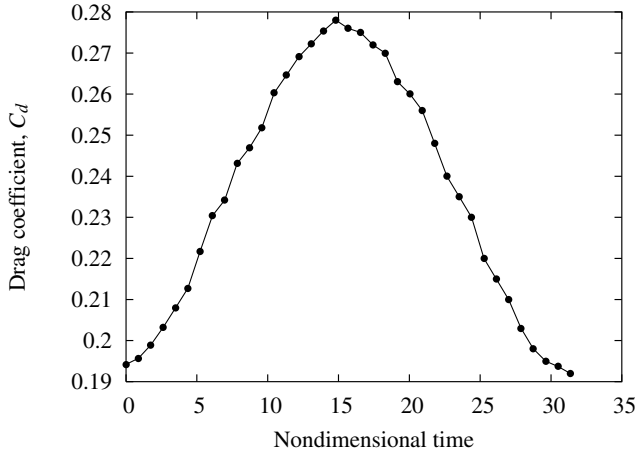

b) Drag coefficient

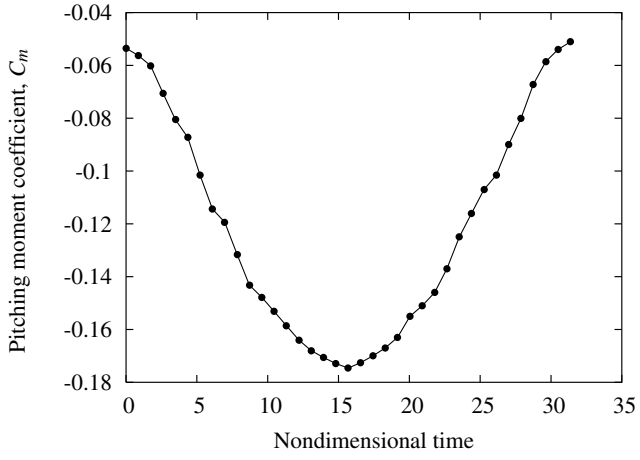

c) Pitching moment coefficient

Fig. 13 Force response amplitude for $\alpha = 15\,\mathrm{deg}$ at $Re = 169,000$.

increased, the distribution of pressure on the airfoil's lower surface changed very significantly and the pressure became increasingly positive, especially near the airfoil's trailing-edge region, but on the airfoil's upper surface the pressure changed very little. Here there is a larger pressure difference between the upper and lower surface of the airfoil. The lift and pitching moment coefficients are significantly increased as shown in Fig. 10. As shown in the instantaneous pressure contours for the nondimensional times from $t^* = 0$ to 15.7, the Gurney flap amplitude increases as the pressure on the lower surface of the airfoil increases. There is a larger region of high pressure on the airfoil's lower surface near the trailing edge.

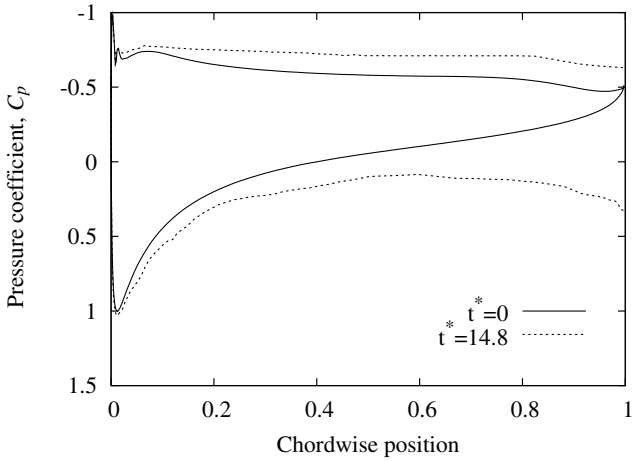

a) Pressure coefficient

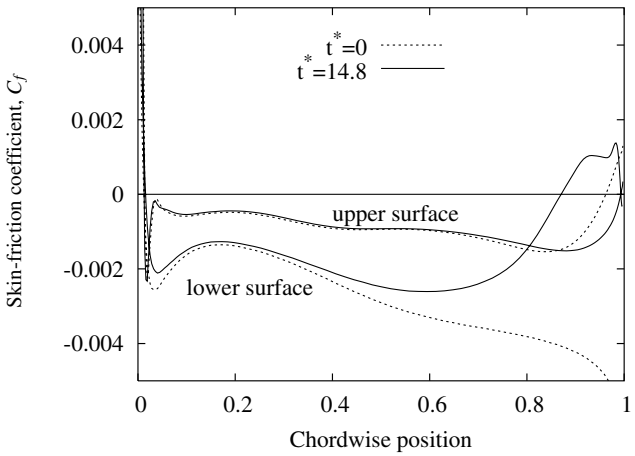

b) Skin friction coefficient

Fig. 14 Pressure and skin-friction responses for $\alpha = 15$ deg at $Re = 169,000$.

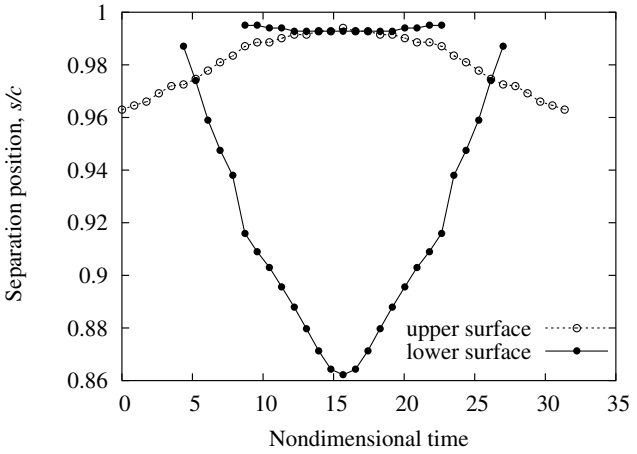

a) Near trailing edge

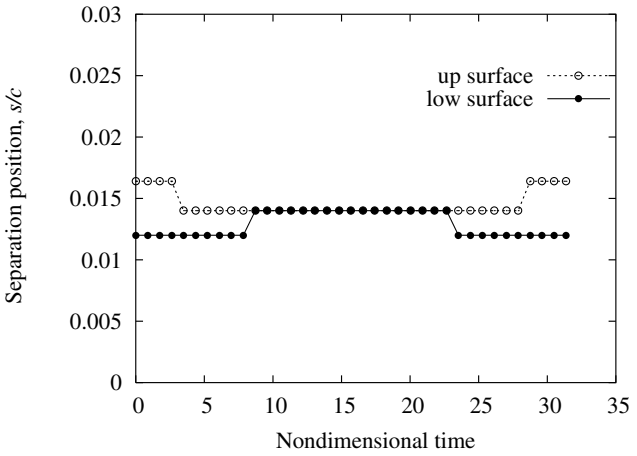

b) Near leading edge

Fig. 15 Unsteady boundary-layer separation for $\alpha = 15$ deg at $Re = 169,000$.

The instantaneous skin-friction coefficients C_f are shown in Fig. 11b for the same conditions as Fig. 11a. The skin friction shows little difference for the upper airfoil surface when the Gurney flap amplitude increases, but for the lower airfoil surface it shows a larger change. The airflow separation points on the airfoil surface can be determined using the sign change of the skin-friction coefficient. A nondimensional chordwise value s/c is used to indicate the airflow separation point position. There are two separation regions, one near the leading edge and the other near the trailing edge. The results are shown in Figs. 12a and 12b.

As shown in Fig. 12a, when the Gurney flap amplitude increases, the variation in the flow separation position near the trailing-edge region is significant, and the separation position moves forward from the trailing edge for the lower airfoil surface and aft for the upper airfoil surface. But the latter has a smaller change. As shown in Fig. 12b, for the separation region near the leading edge very little change occurs for both the upper and lower surfaces. However, for the lower surface there are the multiple separation regions. This may be a numerical artifact due to the skin friction being very close to zero near the leading edge.

The contours of the instantaneous velocity u for the airfoil with the oscillating Gurney flap indicate that for a small Gurney flap amplitude of oscillation there is a small single dynamic stall vortex at the airfoil's trailing edge. With an increase in the Gurney flap amplitude, the vortex region becomes larger and the flow separation points move forward on the lower surface. The larger Gurney flap amplitude causes regions of higher velocity to form outside of the boundary layer on the upper surface of the airfoil. This is due to the increased airfoil circulation that is generated by the Gurney flap.

Results for Sinusoidal Excitation

For the sinusoidal excitation, 36 physical time steps are taken for one period of oscillation. The results are shown in Fig. 13 for the time history of lift, drag, and pitching moment coefficients C_l, C_d, C_m vs. the nondimensional time t^* for $\alpha = 15$ deg. When Gurney flap excitation amplitude is zero ($t^* = 0$), consider the first period in this figure. The transient oscillating process is relatively long. The steady response is reached after 25 time steps (not shown in Fig. 13).

Figure 13 shows the synchronized force response to the Gurney flap excitation when the transient oscillating process of the first period is deleted. The calculation considers one oscillation period of the Gurney flap excitation, and Fig. 13a shows the lift, 13b shows the drag, and 13c shows the pitching moment coefficient responses. The response is an approximate sinusoidal wave. The lift and pitching moment enhancement with the Gurney flap amplitude increase is evident. In addition, there is a significant drag penalty associated with the lift enhancement. In choosing the Gurney flap height one should consider both the lift and drag.

Typical instantaneous surface pressure coefficients C_p are shown in Fig. 14a for the nondimensional times $t^* = 0$ and 14.8 of the Gurney flap oscillating excitation. The results are very similar to those of Fig. 11a for the hyperbolic excitation case. When the Gurney flap amplitude increases, the distribution of pressure on the airfoil's lower surface changed very significantly, especially near the airfoil's trailing-edge region. The pressure changed very little on the airfoil's upper surface.

Typical instantaneous skin-friction coefficients C_f are shown in Fig. 14b for the same conditions as Fig. 14a. The airflow separation

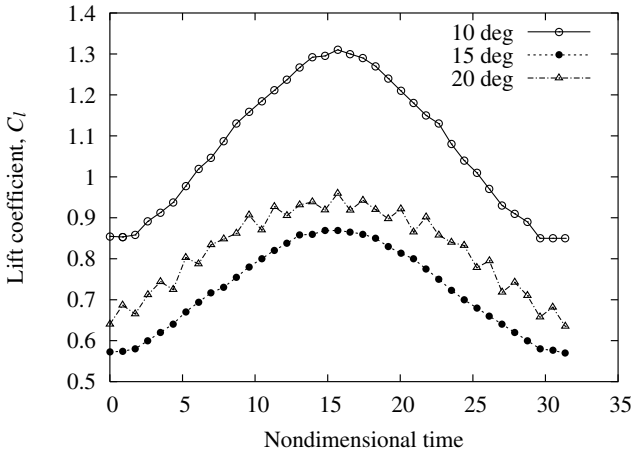

a) Lift coefficient

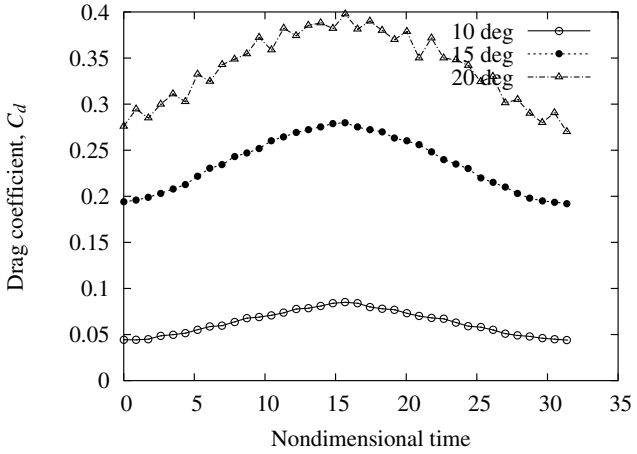

b) Drag coefficient

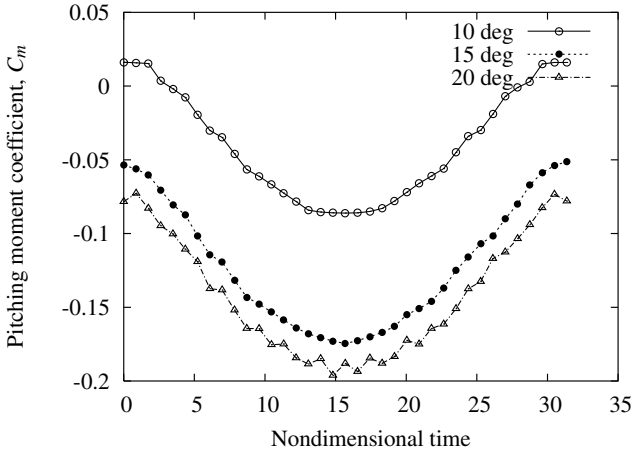

c) Pitching moment coefficient

Fig. 16 Force response amplitude for $\omega = 7.65$ rad/s at $Re = 169,000$.

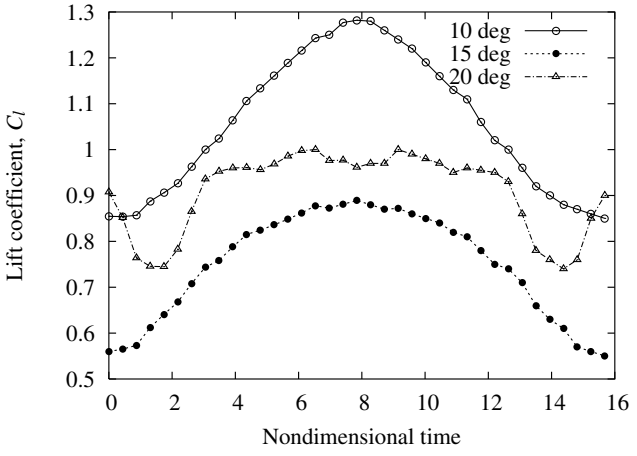

a) Lift coefficient

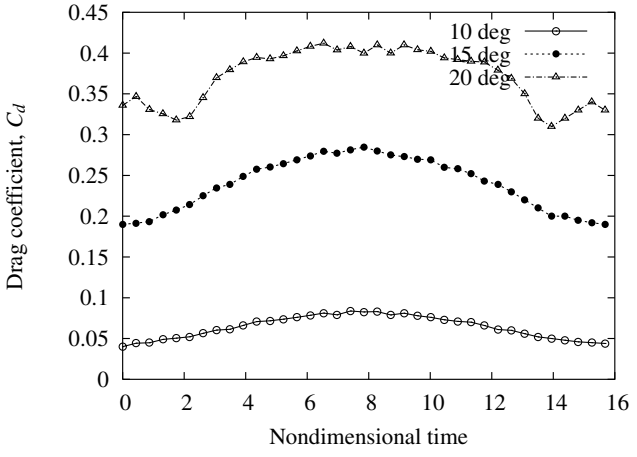

b) Drag coefficient

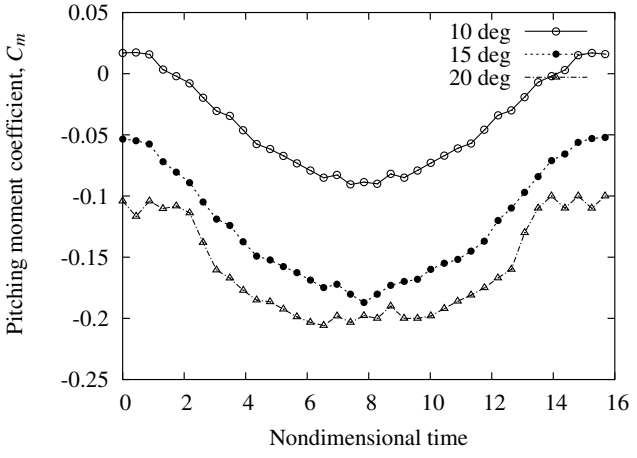

c) Pitching moment coefficient

Fig. 17 Force response amplitude for $\omega = 2 \times 7.65$ rad/s at $Re = 169,000$.

points on the airfoil surface can be seen from this figure. There are two separation regions, one near the leading edge and the other near the trailing edge. The results for the separation position are shown in Figs. 15a and 15b.

As shown in Fig. 15a, when the Gurney flap amplitude increases, the variations in the flow separation position near the trailing-edge region are significant, and the separation position moves forward from the trailing edge for the lower airfoil surface and aft for the upper airfoil surface. Note that there are two trailing-edge separation points on the lower surface for nondimensional times between about 7 and 22. On the other hand, for nondimensional times less than 7 or greater than 22, when the Gurney flap amplitudes are smaller, the effects of GF on the separation point are small. We did not find a second flow separation point in this case. But for larger GF amplitude (between the nondimensional times 7 and 22), the effects will be not small. Thus a new flow separation point arises near the GF location.

Also there is a separation region near the location of the Gurney flap, but it is small. As shown in Fig. 15b, for the separation region near the leading edge, very little change occurs for either the upper or lower surfaces.

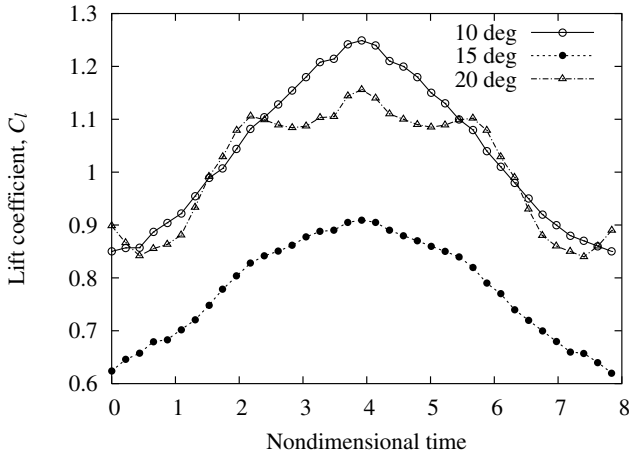

a) Lift coefficient

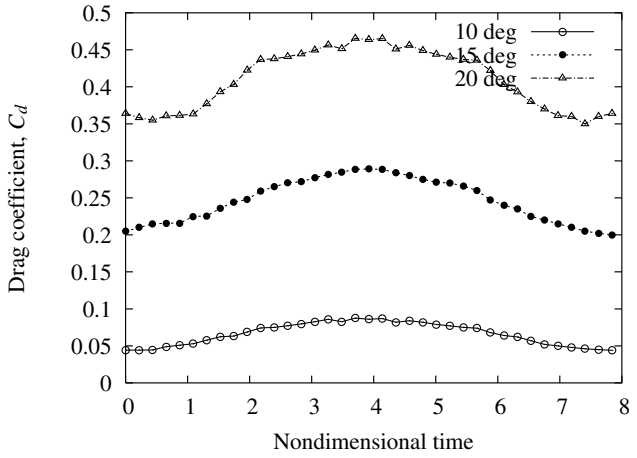

b) Drag coefficient

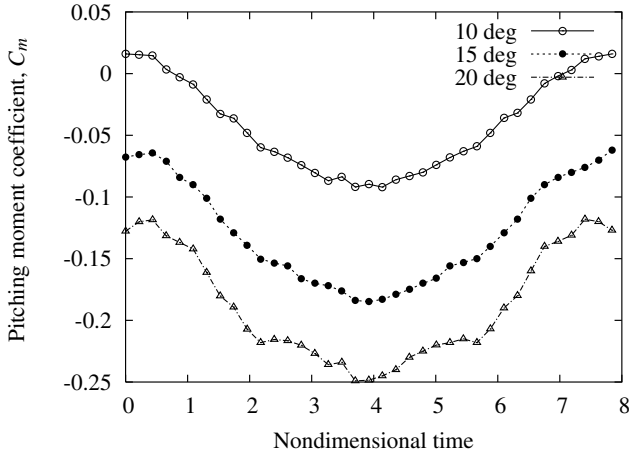

c) Pitching moment coefficient

Fig. 18 Force response amplitude for $\omega = 4 \times 7.65$ rad/s at $Re = 169,000$.

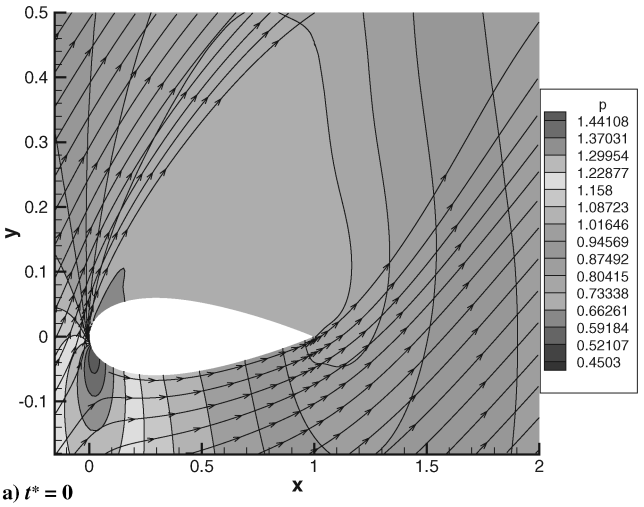

a) $t^* = 0$

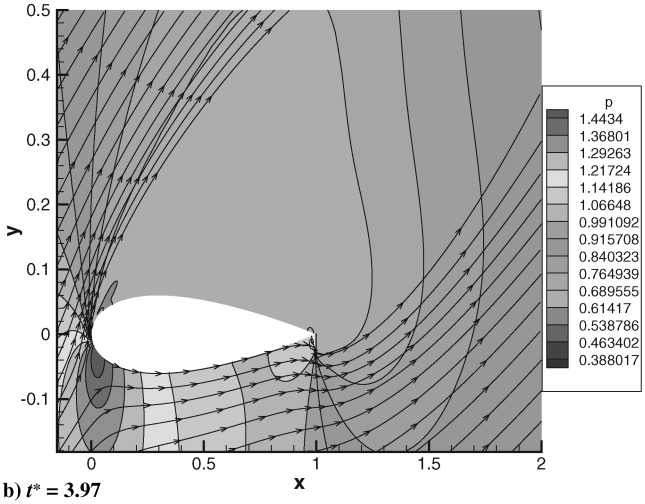

b) $t^* = 3.97$

Fig. 19 Streamlines and pressure contours for $\alpha = 20$ deg and the Gurney flap excitation frequency $\omega = 2 \times 7.65$ rad/s at $Re = 169,000$. Note the y scale has been exaggerated for clarity.

Now we discuss the effects of the angle of attack and the Gurney flap oscillating frequency on the unsteady flow aerodynamic load for the sinusoidal excitation of the Gurney flap. Three typical angles of attack are considered, that is, $\alpha = 10$ deg for a below-stall angle, $\alpha = 15$ deg for a slight-stall angle, and $\alpha = 20$ deg for a deep-stall angle. Three oscillation frequencies of the Gurney flap are considered. In addition to the baseline oscillating frequency $\omega = 7.65$ rad/s, 2ω and 4ω are also chosen. The results are presented in Figs. 16–18.

For comparison, the results of three different angles of attack are plotted in Figs. 16–18. When $\alpha = 10$ deg (below-stall angle), the response of the aerodynamic load has a sinusoidal motion. The averaged response amplitude is $C_l = 1.085$ for the lift coefficient, an increase of 26.16% compared with a static airfoil without the Gurney flap. The averaged drag coefficient C_d is 0.064, an increase of 46%, and the averaged pitching moment coefficient $C_m = -0.051$, an increase of about 3 times compared with a static airfoil. The pitching moment increase is accompanied by a substantial increase in a nose-down component. The results for $\alpha = 15$ deg (slight-stall angle) have been discussed before. For ready reference, the results are also plotted in these figures. When $\alpha = 20$ deg (deep-stall angle), the response of the aerodynamic load becomes complex. In addition to a fundamental frequency response, there are some higher harmonic components. The averaged response amplitudes are $C_l = 0.805$, $C_d = 0.33$, and $C_m = -0.13$. By comparison, for a static airfoil without the Gurney flap, $C_l = 0.64$, $C_d = 0.276$, and $C_m = -0.08$. A 25.8% increase in the C_l, 16.36% increase in the C_d, and 38.4% increase in the C_m have been achieved. The addition of an oscillating Gurney flap brings significant benefit for the deep-stall aerodynamics, because of a significant increase in the dynamic lift and pitch moment coefficients with only a small increase in the drag coefficient.

The instantaneous streamlines superimposed on the flowfield pressure contours for the airfoil at the nondimensional times $t^* = 0$ (19a), that is, corresponding to the zero Gurney flap amplitude, and $t^* = 3.97$ (19b), that is, corresponding to the maximum Gurney flap amplitude, are shown in Figs. 19a and 19b for $\alpha = 20$ deg and the Gurney flap excitation frequency $\omega = 2 \times 7.65$ rad/s, respectively. As shown in Fig. 19a, the leading edge separation is moved forward

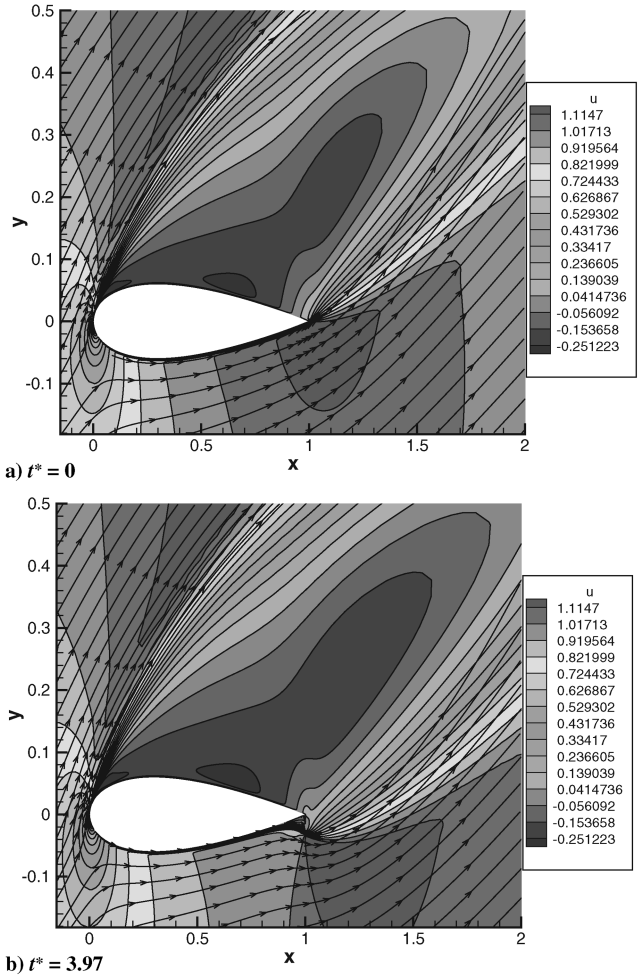

a) $t^* = 0$

b) $t^* = 3.97$

Fig. 20 Streamlines and velocity u contours for $\alpha = 20$ deg and the Gurney flap excitation frequency $\omega = 2 \times 7.65$ rad/s at $Re = 169,000$. Note the y scale has been exaggerated for clarity.

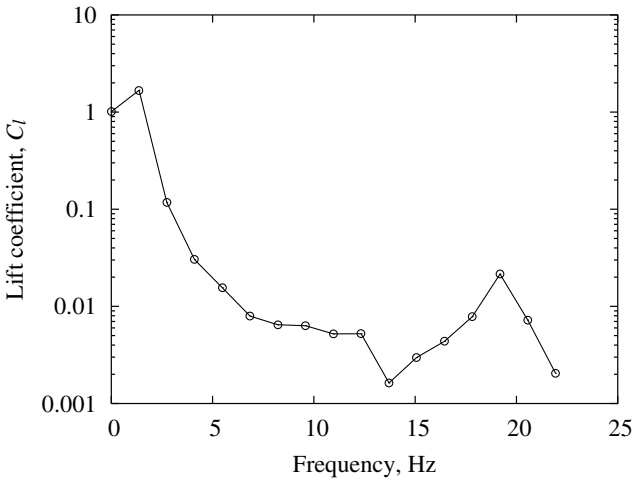

a) $\omega = 7.00$ rad/s

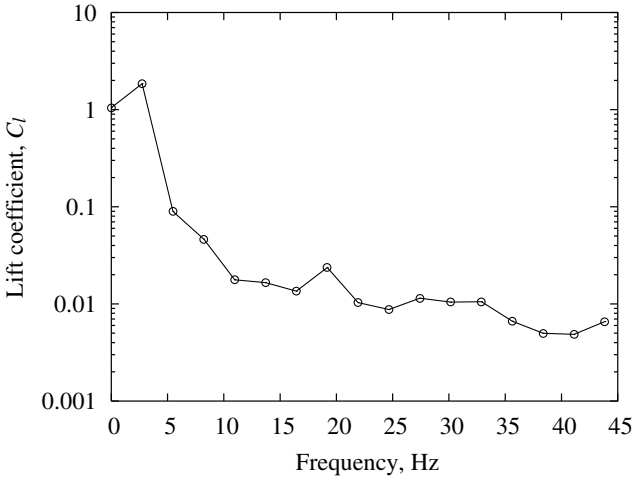

b) $\omega = 2 \times 7.00$ rad/s

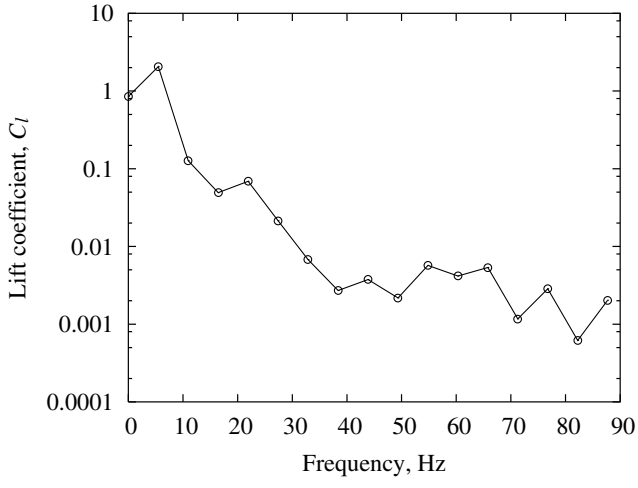

c) $\omega = 4 \times 7.00$ rad/s

Fig. 21 FFT analysis of lift response at three different oscillating frequencies of the Gurney flap.

to almost $s/c \sim 0$, and the reattachment is moved aft to near the trailing edge ($s/c \sim 1$). The separation bubble has detached from the airfoil upper surface to form the expected dynamic stall vortex. In this region, the upper surface pressure decreases and that leads to a smaller lift and a larger drag on the airfoil. As shown in Fig. 19b, for the addition of a Gurney flap, there is a larger region of high pressure on the airfoil's lower surface and a decreased pressure region on the upper surface compared with the clean airfoil case. The addition of a Gurney flap generates a region of higher pressure on the lower surface at the trailing edge that leads to an increase in the nose-down pitching moment. This is an expected result also found in previous research on steady flows [13].

Corresponding to Figs. 19a and 19b, the contours and streamlines of the instantaneous velocity u are presented in Figs. 20a and 20b for the airfoil at the nondimensional times $t^* = 0$ and $t^* = 3.97$, respectively. As shown in Fig. 20a, there is a very large region of reversed flow on the upper surface. In the reversed flow region, the stall vortices that are associated with the clockwise vortex near the leading edge and associated with the counterclockwise vortex near $s/c = 0.5 \sim 0.7$ can be seen. As shown in Fig. 20a and 20b, with the addition of a Gurney flap, three primary effects are observed. First, the Gurney flap causes a region of higher velocity to form outside of the boundary layer on the upper surface of the airfoil. This is due to the increased airfoil circulation that is generated by the Gurney flap. The second effect of the Gurney flap is to pull the wake downward. This is seen from the downward shift in the contour near the Gurney flap when Figs. 20a and 20b are compared. Finally, the stagnation point is slightly shifted toward the lower airfoil surface due to the Gurney flap, as can be seen by comparing Figs. 20a and 20b.

When the oscillating frequency of the Gurney flap increases, the aerodynamic forces have a small change for $\alpha = 10$ deg and $\alpha = 15$ deg. However, for the deep-stall case ($\alpha = 20$ deg), the response change is significant and the benefit of the Gurney flap increases as the oscillating frequency increases. To better understand this phenomenon, Fig. 21 shows an FFT analysis of the lift response for $\alpha = 20$ deg and different oscillating frequencies. There is a

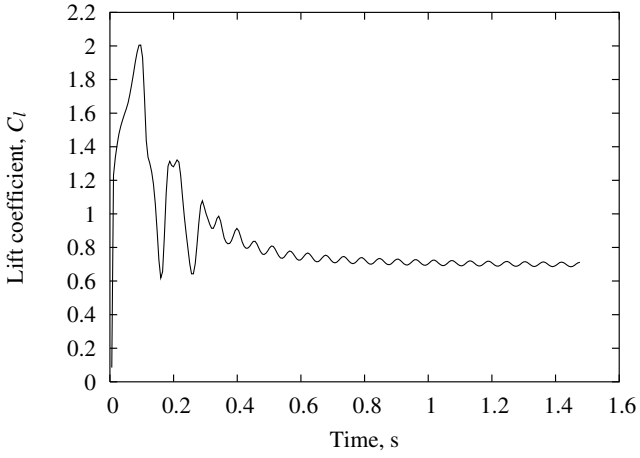

a) Lift coefficient

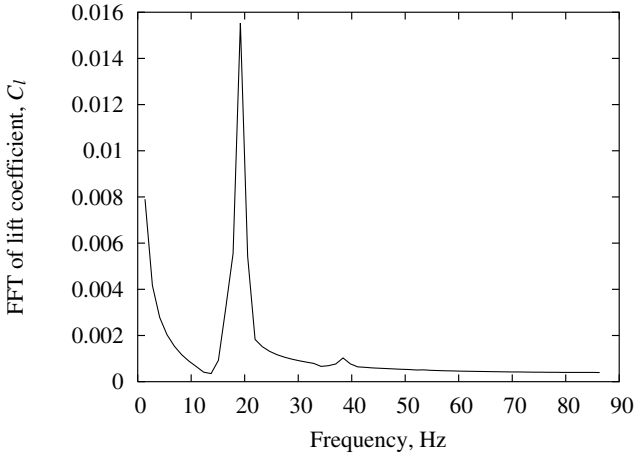

b) FFT analysis

Fig. 22 Lift response amplitude and FFT analysis for the free transient vibration process at $Re = 169,000$.

significant higher harmonic frequency component at $\omega = 19.5$ Hz or near 19.5 Hz for these three excitation frequencies. This frequency may be created by a von Karman vortex street when deep stall occurs. The von Karman vortex structure can be seen from Fig. 20a. This frequency is called a vortex shedding (or flow oscillation) frequency. During deep stall, the usual bluff-body shedding occurs at a Strouhal number $St_s \approx 0.2$. Thus, an approximate von Karman vortex shedding frequency can be estimated from Strouhal number St_s

$$St_s \equiv \frac{f_s c \sin\alpha}{U_\infty} \approx 0.2$$

where U_∞ is the freestream mean flow velocity (m/s). In the present example, $Re = 169000$, $c = 0.254$ (m), $\alpha = 20$ deg, and $U_\infty = 9.7$ (m/s). Thus, $f_s \approx 22.34$ Hz, which is quite close to the value of 19.5 Hz. $c \sin\alpha$ is the effective cross-sectional dimension of the bluff body for the airfoil at large α.

To further confirm the present analysis, a physical time transient free response and corresponding FFT analysis are shown in Figs. 22a and 22b for $\alpha = 20$ deg and the zero Gurney flap amplitude. The maximum number of time steps is $N_{t\max} = 256$ and the physical time step is $\Delta t = 0.0057$ (s). As shown in Fig. 22a, the free oscillation response consists of an initial transient vibration process and a steady oscillation response with a small amplitude. This is a shedding-free oscillation caused by the von Karman vortex street. The FFT analysis of this steady free oscillation response is shown in Fig. 22b. The dominant frequency (i.e., shedding frequency f_s), is 19.5 Hz.

From the preceding calculation, it is expected that when the oscillating frequency of the Gurney flap is in the range of this vortex shedding frequency, the benefit of the Gurney flap will be increased.

Concluding Remarks

Unsteady aerodynamic flow passive control based on an oscillating airfoil with small trailing-edge strips (or Gurney flaps) and an oscillating Gurney flap with fixed airfoil were theoretically studied using a Navier–Stokes code, INS2D, and the following conclusions were drawn:

1) A Gurney flap on an oscillating airfoil can significantly increase the maximum dynamic lift and stall angle of attack. The experimental data of Gerontakos and Lee [13] for the dynamic-lift hysteresis loop support the present computational results.

2) The computational results for the oscillating Gurney flap with fixed airfoil show that the addition of an oscillating Gurney flap brings significant benefit for the case of deep-stall aerodynamics ($\alpha = 20$ deg) by providing a significant increase in the dynamic lift and pitching moment coefficients with only a small increase in the drag coefficient. For slight-stall conditions ($\alpha = 15$ deg), the Gurney flap provided larger lift and pitching moment enhancements with a larger drag penalty.

3) The present computational investigation can be used as a guide for an experimental investigation of active aerodynamic flow control of a wing with an oscillating Gurney flap.

Acknowledgements

This work was supported under the Air Force Office of Scientific Research (AFOSR) grant "Dynamic and Control of Nonlinear Fluid-Structure Interaction" under the direction of Dean Mook and Clark Allred. We would like to thank Peter Attar for his participation in the theoretical calculations.

References

[1] Liebeck, R. H., "Design of Subsonic Airfoil for High Lift," *Journal of Aircraft*, Vol. 15, No. 9, 1978, pp. 547–561.

[2] Jeffrey, D., Zhang, X., and Hurst, D. W., "Aerodynamics of Gurney Flaps on a Single-Element High-Lift Wing," *Journal of Aircraft*, Vol. 37, No. 2, 2000, pp. 295–301.

[3] Van Dam, C. P., Yen D. T., and Vijhen, P. M. H. W., "Gurney Flap Experiments on Airfoil and Wings," *Journal of Aircraft*, Vol. 36, No. 2, 1999, pp. 484–486.

[4] Storms, B. L., and Jang, C. S., "Lift Enhancement of an Airfoil Using a Gurney Flap and Vortex Generators" *Journal of Aircraft*, Vol. 31, No. 3, 1994, pp. 542–547.

[5] McCroskey, W. J., "Unsteady Airfoils," *Annual Review of Fluid Mechanics*, Vol. 14, Jan. 1982, pp. 285–311.

[6] Carr, L. W., "Progress in Analysis and Prediction of Dynamic Stall," *Journal of Aircraft*, Vol. 25, No. 1, 1988, pp. 6–17.

[7] Carr, L. W., and McCroskey, W. J., "A Review of Recent Advances in Computational and Experimental Analysis of Dynamic Stall," *Proceedings of IUTAM Symposium on Fluid Dynamics of High Angle of Attack*, Springer–Verlag, New York, 1993, pp. 3–31.

[8] Carr, L. W., and Chandrasekhara, M. S., "Compressibility Effects on Dynamic Stall," *Progress in Aerospace Sciences*, Vol. 32, Dec. 1996, pp. 523–573.

[9] Aso, S., and Hayashi, M., "Experimental and Computational Studies on Dynamic Stall in Low Speed Flows," *Proceedings of IUTAM Symposium on Fluid Dynamics of High Angle of Attack*, Springer–Verlag, New York, 1993, pp. 67–78.

[10] Badcock, K. J., Cantariti, F., Hawkins, I., Woodgate, M., Dubuc, L., and Richards, B. E., "Simulation of Unsteady Turbulent Flows Around Moving Airfoils Using the Pseudo-Time Method," *International Journal for Numerical Methods in Fluids*, Vol. 32, No. 5, Feb. 2000, pp. 585–604.

[11] Greenblatt, D., and Wygnanski, I., "Dynamic Stall Control by Periodic Excitation, Part 1: NACA0015 Parametric Study," *Journal of Aircraft*, Vol. 38, No. 3, 2001, pp. 430–438.

[12] Greenblatt, D., Neuburger, D., and Wygnanski, I., "Dynamic Stall Control by Intermittent Periodic Excitation," *Journal of Aircraft*, Vol. 38, No. 1, 2001, pp. 188–190.

[13] Gerontakos, P., and Lee, T., "Oscillating Wing Loadings with Small Trailing-Edge Strips," *Journal of Aircraft*, Vol. 43, No. 2, 2006, pp 428–436.

[14] Stuart, E. R., and Dochan, K., "An Upwind Differencing Scheme for the Time-Accurate Incompressible Navier–Stokes Equations," *AIAA Journal*, Vol. 28, No. 2, 1990, pp. 253–262.